

Appendix B

The Space Environment

B.1 Introduction to Space Environments

This Appendix is intended to supplement the material presented in Chapter 2. It presents many of the concepts introduced in Chapter 2 in more detail for the interested reader.

B.1.1 Quantitative Representations of the Space Environment

Earth's plasma is properly described in terms of a so-called phase space density or distribution function. Space plasmas can be described most simply in terms of the Maxwell-Boltzmann distribution. As this representation lends itself to efficient manipulation when carrying out charging calculations, it is often the preferred way for describing plasmas. The Maxwell-Boltzmann distribution F_i is given by:

$$F_i(v) = [n_i \{m_i / (2\pi k T_i)\}^{3/2}] \exp\{-m_i v^2 / (2k T_i)\} \quad (\text{B.1-1})$$

where:

- n_i = number density of species i
- m_i = mass of species i
- k = Boltzmann constant
- T_i = characteristic temperature of species i
- v = velocity
- F_i = distribution function of species i

Unfortunately, the space plasma environment is seldom a Maxwell-Boltzmann distribution. However, given the actual plasma distribution function, it is possible to define (irrespective of whether the plasma is Maxwell-Boltzmann or not) moments of the particle distribution that reveal characteristics of its shape. In most cases, these moments can then be used to determine an approximate Maxwell-Boltzmann distribution. The first four of these characteristic moments are:

$$\langle ND_i \rangle = 4\pi \int_0^{\infty} (v^0) F_i v^2 dv \quad (\text{B.1-2})$$

$$\langle NF_i \rangle = \int_0^{\infty} (v^1) F_i v^2 dv \quad (\text{B.1-3})$$

$$\langle ED_i \rangle = (4\pi m_i/2) \int_0^{\infty} (v^2) F_i v^2 dv \quad (\text{B.1-4})$$

$$\langle EF_i \rangle = (m_i/2) \int_0^{\infty} (v^3) F_i v^2 dv \quad (\text{B.1-5})$$

where:

$$\langle ND_i \rangle = \text{number density of species } i$$

$$\langle NF_i \rangle = \text{number flux of species } i$$

$$\langle ED_i \rangle = \text{energy density of species } i$$

$$\langle EF_i \rangle = \text{energy flux of species } i$$

For the Maxwell-Boltzmann distribution of Eq. (B.1-1), these assume the following values:

$$\langle ND_i \rangle = n_i \quad (\text{B.1-6})$$

$$\langle NF_i \rangle = (n_i/2\pi)(2kT_i/\pi m_i)^{1/2} \quad (\text{B.1-7})$$

$$\langle ED_i \rangle = (3/2)n_i k T_i \quad (\text{B.1-8})$$

$$\langle EF_i \rangle = (m_i n_i/2)(2kT_i/\pi m_i)^{3/2} \quad (\text{B.1-9})$$

It is often easier to measure the moments (e.g., number flux, of the plasma distribution function) than the actual distribution function in terms of energy or the temperature. This is particularly true for space plasmas where the concept of temperature is not well defined. As an illustration, from the first four moments,

two definitions of the plasma temperature consistent with a Maxwell-Boltzmann distribution are possible as follows:

$$T_{av} = 2\langle ED \rangle / 3\langle ND \rangle \quad (\text{B.1-10})$$

$$T_{rms} = \langle EF \rangle / 2\langle NF \rangle \quad (\text{B.1-11})$$

For a true Maxwell-Boltzmann plasma, these quantities would be equal; for actual plasmas, T_{rms} is usually greater than T_{av} . Even so, experience has shown that a representation in terms of two Maxwell-Boltzmann distributions is, in fact, a better mathematical representation of the space plasma than a single Maxwellian. That is, the plasma distribution for a single species can be represented by:

$$F_2(v) = \{m/(2\pi k)\}^{3/2} [\{N_1/(T_1)^{3/2}\} \\ \times \exp(-mv^2/2kT_1) + \{N_2/(T_2)^{3/2}\} \exp(-mv^2/2kT_2)] \quad (\text{B.1-12})$$

where:

N_1 = number density for population 1

T_1 = temperature for population 1

N_2 = number density for population 2

T_2 = temperature for population 2

In most cases, this representation fits the data quite adequately over the energy range of importance to spacecraft surface charging, namely, ~ 1 eV to 100 keV. Further, it is very simple to derive N_1 , T_1 , N_2 , and T_2 directly from the four moments so that a consistent mathematical representation of the plasma can be established that incorporates the simplicity of the Maxwell-Boltzmann representation while maintaining a physically reasonable picture of the plasma. The distinction between T_{av} , T_{rms} , T_1 , and T_2 must be kept in mind, however, whenever reference is made to a Maxwell-Boltzmann distribution, as this is only an approximation at best to the actual plasma environment.

Although the Maxwell-Boltzmann distribution can be used for representing the high-energy electron environment for internal charging, it is typically not as useful as it is for surface charging calculations. More typically, the electron environment above ~ 100 keV approaches a functional form represented by a power law or the more complex Kappa distribution which better represents the non-thermal tail in the electron distribution at higher energies. For example, if a

power law distribution $A_0 E^{-X}$ is assumed for $i(E)$, the differential intensity (also often called “flux”), the integral intensity ($I(E)$) would give:

$$I(E) = - \int_E^{\infty} i(E) dE = -(A_0 E^{1-X})/(1 - X) \quad (\text{B.1-13})$$

where:

$i(E)$ = $-dI(E)/dE$ = differential angular intensity (or flux) = particles per unit area per unit energy per unit of solid angle at energy E
(example: $\text{n\#/cm}^2\text{-s-sr-keV}$)

$I(E)$ = integral (over energy) angular intensity (or flux) = particles per unit area per unit of solid angle from energy E to infinity
(example: $\text{n\#/cm}^2\text{-s-sr}$)

E = energy of particle

A_0, X = constants

The omnidirectional fluxes are then given by

$$j(E) = \int_0^{\pi} d\alpha \int_0^{2\pi} i(E) \sin(\alpha) d\phi \quad (\text{B.1-14})$$

$$J(E) = \int_0^{\pi} d\alpha \int_0^{2\pi} I(E) \sin(\alpha) d\phi \quad (\text{B.1-15})$$

where:

$j(E)$ = omnidirectional differential flux = particles per unit area per unit energy integrated over 4π steradians at energy E (example: $\text{n\#/cm}^2\text{-s-MeV}$)

$J(E)$ = omnidirectional integral flux = particles per unit area over 4π steradians from energy E to infinity (example: $\text{n\#/cm}^2\text{-s}$)

α = particle pitch angle (radians) for particles in a magnetic field or, in the absence of a magnetic field, the angle relative to the normal to a surface

Some publications, including NASA’s AE8/AP8 family of radiation models, use the term omnidirectional integral flux as defined above, which implies an isotropic (uniform in all directions) particle flux. This is our J or the omnidirectional integral flux. Other publications report intensity (flux) per

steradian (or our I with units of $\#/cm^2\text{-s-sr}$). Assuming an isotropic plasma (a common simplifying assumption), the two are related by:

$$J = 4 \pi I \quad (\text{B.1-16})$$

Similarly, after multiplying by charge, q , and converting from charge/s to amperes, the net current per unit area, J , to a flat surface for an isotropic flux, when integrated over angle (Eq. B.1-15) can be shown to be:

$$J = \pi q I \quad (\text{B.1-17})$$

$$\text{units: } A/cm^2$$

The reduction of $1/4$ is due to two factors. The first $1/2$ is because the current to a surface only comes from one side of the surface. The second $1/2$ is the average value of current due to the integral over angle for non-normal incidence. If the flux is not isotropic, these simple calculations must be redone for the actual angular distribution.

[Note: to avoid confusion, in the rest of the book, the current to a spacecraft will be defined as “ I ” where $I = J \times (\text{collection area})$.]

The preceding is true for the fluxes and currents impacting the surface. For penetration calculations, the geometry of the shielding must be carefully considered in estimating the fluxes in a material or inside the shielding. For example, the non-normally incident electrons cannot penetrate as deep as normally incident electrons because of the longer path length through the shielding to a given point. The difference depends on the depth and on the spectrum of the electrons; accurate calculations require specialized codes which will be discussed later in the appendices.

B.1.2 Data Sources

The following subsections briefly list the satellites and sources from which environmental data can be obtained. Note that there are problems in attempting to obtain calibrated particle data from space. Energetic electron detector data are, as an example, sometimes affected by the presence of energetic protons that generate secondary electrons during their passage through the detector. Detectors may degrade and become less efficient over time or may not even be initially calibrated over all energy ranges. View factors and orientation relative to the magnetic field also contribute to uncertainties in the count rate to flux conversion. Despite these concerns, the errors are usually small enough to permit the data to be used in estimating charging, at least for engineering purposes.

B.1.2.1 AT5-5, AT5-6

A major source of data on the geosynchronous plasma environment has been the University of California at San Diego (UCSD) low-energy plasma detectors on the NASA geosynchronous satellites AT5-5 and AT5-6. In particular, data were taken for electrons and ions (assumed to be protons) in 62 energy channels. For AT5-5, at a longitude of ~ 225 deg E, spectra were taken every 20 s in 112 percent (dE/E) energy intervals from 51 eV to 51 KeV. For AT5-6, at a longitude of ~ 266 deg E, spectra were taken every 15 s in 113-percent dE/E intervals from 1 eV to 81 KeV. The data are available from the National Space Science Data Center (NSSDC) in 10-min average bins for 50 days between 1969 and 1970 for AT5-5 and 10-min bins for 45 days between 1974 and 1976 for AT5-6. The data are in the form of observation time, spacecraft coordinates, and the four moments of the electron and ion distribution functions. These data were analyzed extensively in papers by Garrett, DeForest, and their colleagues[1–3]. They, along with data from SCATHA, represented the primary source of statistical data on the geosynchronous orbit until recent studies of the Los Alamos National Laboratory (LANL) instruments (B.1.2.4). An additional 10 days of data from AT5-6 are also available for a unique period (September 14–25, 1976), during which the AT5-6 spacecraft passed by the LANL Charged Particle Analyzer (CPA) instrument on another geosynchronous spacecraft allowing careful cross-calibration of the particle instruments. Some descriptions of these data appear in reference [4]. Reference [5] provides an excellent summary of Earth’s space plasma environments that sets the context for these observations.

B.1.2.2 SCATHA

Launched in 1979, the SCATHA satellite is another major source of spacecraft charging data. In addition to numerous experiments for measuring and controlling spacecraft charging, SCATHA measured the space environment between 5.5 and 7.7 R_e for a number of years. Of particular interest to environmental studies are the Air Force Geophysics Laboratory (AFGL) SC5 Rapid Scan Particle Detector, which measured the electron and ion environments at 1 s intervals over the range of 50 eV to 0.5 MeV, and the UCSD SC9 Low Energy Plasma Detector, which measured the electron and ion plasma every 0.25 s at energies of 1 eV to 81 KeV, the instrument being a near-duplicate of the AT5-5 and AT5-6 instruments. As in the case of these two spacecraft, the data were extensively analyzed by Mullen, Garrett, and their colleagues to return similar statistical results that can be compared to the AT5-5 and AT5-6 findings [6–9]. The data are available in the referenced documents and some through the NSSDC.

B.1.2.3 GOES

The most readily available data on the high-energy particle environments are those from the National Oceanic and Atmospheric Administration (NOAA) Geosynchronous Operational Environmental Satellite (GOES) series of spacecraft at geosynchronous orbit. The data of interest here consist primarily of $E > 2$ MeV electron fluxes expressed in $\text{e-cm}^{-2}\text{-s}^{-1}\text{-sr}^{-1}$. Starting with GOES 8, data are also available for the $E > 600$ keV electron environment. Data from at least early 1986 to the present are readily available. GOES satellites are generally positioned over the United States East and the West Coasts, but their exact positions have varied over the years. Contact Dan Wilkinson, phone 303-497-6137. Data are available in near real time over the worldwide web at: <http://ngdc.noaa.gov/>; click on “Space Weather & Solar Events,” then click on “Satellite Data Services: GOES SEM” and select from various options. Alternatively, at the home page, look at various selection options. Go to URL <http://www.swpc.noaa.gov/today.html> for the last 3 days of GOES space weather data.

B.1.2.4 Los Alamos Detectors

Detectors on board various Department of Defense (DoD) geosynchronous spacecraft provided by the LANL have been in service since the 1970s. Higher energy channels are referred to as CPA or, currently, the SOPA experiments. The data cover a wide energy range (e.g., from $E > 30$ eV to $E > 5$ MeV for electrons) and are available from 1976 through 2005. The data are well calibrated and provide a more detailed snapshot of the environment than the GOES data but have not been as readily available. Recent papers presenting the Los Alamos data are references [10] and [11]. Contact Michelle Thomsen, phone 506-667-1210, or Geoff Reeves, phone 505-665-3877. The LANL data web site can be accessed at: <http://leadbelly.lanl.gov/>. Historical to current energetic particle data can be obtained at that site.

In addition to SOPA, since 1989, LANL has been accumulating high-quality measurements of electron and proton energy flux spectra from 1 eV to 40 keV from Magnetospheric Plasma Analyzer (MPA) instruments aboard a series of geosynchronous spacecraft. These data not only characterize the plasma but can also be used to infer the potential (relative to plasma) of the instrument ground and the presence of differential charging. From the raw data, spin-angle-averaged flux spectra, spacecraft potential, and various moments are computed. The density and temperature moments should be used cautiously with a full understanding of how they are computed (see [12] for details of the data analysis). Reference [13] provides statistics on the electrons and ions over a full solar cycle along with detailed spectra. Spectrograms and moments can be

obtained from Michelle Thomsen at mthomsen@lanl.gov for further information and specific data.

B.1.2.5 CRRES

Launched in 1990, the Combined Release and Radiation Effects Satellite (CRRES) spacecraft provided the most accurate and detailed measurements of Earth's radiation belts in many decades. A landmark in internal charging (it carried the first experiment specifically designed to study internal charging), it provided extensive data on the location and occurrence of IESDs throughout the magnetosphere. CRRES was launched into an eccentric, 18 deg inclination orbit that took it from below the Van Allen belts out to geosynchronous orbit. It had an orbital period of 10 hr and measured from a few eV to 10 MeV electrons. The primary data are from July 25, 1990, to October 1991, and include extensive measurements of internal arcing rates in addition to the radiation data. These data and related software codes may be obtained via a Google search of AF-GEOSPACE; use link Fact Sheets: AF-GEOSPACE; a software request form is provided.

B.1.2.6 Solar, Anomalous, and Magnetospheric Particle Explorer (SAMPEX)

Launched in 1992, SAMPEX has returned a wealth of data on the low altitude radiation environment. The satellite is in a high inclination (82 deg) polar orbit with an altitude of 520×670 km. Its orbit passes through many L-shells, and its data, although not from a high altitude, contain information from those L-shells. The SAMPEX Proton/Electron Telescope (PET) provides measurements on precipitating electrons from 0.4 to ~30 MeV over the polar regions. Contact Dr. Dan Baker, phone 303-492-0591.

B.1.2.7 Other Sources

The NASA International Solar-Terrestrial Physics (ISTP) program has several satellites in orbit that are useful for specific orbits, e.g., plasma conditions in the solar wind or in Earth's magnetotail. A web site is <http://www-istp.gsfc.nasa.gov>. The European satellite, Giove-A has a simple but elegant experiment, Merlin, on board that measures electron flux and other plasma parameters. Ryden [14] and more recent papers by him and others describe excellent results from this MEO satellite.

For anomaly investigations, it is desirable to determine quickly what the state of the electron environment was during the event. No appropriate plasma data may be available for either that time period or for the particular spacecraft orbit. In that case, possible secondary sources are the geomagnetic indices or anomaly data from other spacecraft in orbit at the same time. These data are also of value

as support material in carrying out anomaly investigations as they may allow identification of the actual cause such as surface charging or single event upsets (SEUs). NOAA's World Data Center (WDC) at Boulder, Colorado, provides a number of useful indices on a near real-time basis and maintains a spacecraft anomaly database. These materials can be addressed through the web at: <http://www.ngdc.noaa.gov/wdc/>.

Interest is increasing in the development of a simple universal space environment detector for flight on commercial spacecraft to monitor surface and internal charging fluxes. The International Telecommunications Satellite Organization (INTELSAT) has flown at least one such device; others have been flown as well. If a net of such sensors should become available, it might be possible to provide real-time measurements of the state of Earth's plasma and radiation environments and forecast surface and internal discharging effects.

B.2 Geosynchronous Environment

B.2.1 Geosynchronous Plasma Environments

In this section, the geosynchronous plasma environment is described in terms of temperature and number density. This simple characterization of the environment assumes two species, electrons and protons, where the energy distribution of each species is described by the Maxwell-Boltzmann distribution (Appendix B.1.1). This treatment is used because the Maxwell-Boltzmann function can be easily used in calculating spacecraft charging. If the Maxwell-Boltzmann distribution is not used, actual data should be curve fit digitally and integrated numerically at a much greater computational cost. If a single Maxwell-Boltzmann distribution is inadequate for a given circumstance, the measured data are often treated as the sum of two Maxwell-Boltzmann populations. Species such as oxygen and helium can be included as additional Maxwellian populations. Note: Other representations such as a Kappa distribution are also possible, but the Maxwell-Boltzmann distribution is adequate for most simple charging estimates.

The following text describes in greater detail the characterization of the geosynchronous plasma environment in terms of Maxwell-Boltzmann distribution and its moments. The interested reader is also referred to more recent studies of the charging environment using data from the LANL electron and ion spectrometers on a number of geosynchronous spacecraft. See for example [13] and [12] for the ~ 1 eV to ~ 45 keV electron and ion environments and [10] for the corresponding 30 keV-2.5 MeV electron environment (the "POLE" model). Reference [11] has merged the LANL data with data from the

Japanese Data Relay Test Satellite to cover the range from 1 keV to 5.2 MeV (the “IGE-2006” model).

An initial step in characterizing environments is to consider averages. Ten-min averages of approximately 45 days per spacecraft were estimated from the ATS-5, ATS-6, and SCATHA (experiment SC9) spacecraft. The corresponding averages (Table B-1) and standard deviations (Table B-2) for each spacecraft were then estimated. The ions were assumed to be protons in these tables. Note that, in many cases, the standard deviation exceeded the average. This resulted from the great variability of the geosynchronous environment and illustrates the inherent difficulty of attempting to characterize the “average” plasma environment. (Another way of characterizing the data that avoids some of these problems is to assume that the data are statistically log-normally distributed.) These values are useful, however, in estimating the mean or pre-storm conditions that a spacecraft will experience, as the initial charge state of a spacecraft is important in determining how the vehicle will respond to a significant environmental change. Also, these averages give an approximate idea of how plasma conditions vary over a solar cycle since the ATS-5 data are for 1969-70, the ATS-6 data for 1974-76, and the SCATHA data for 1978.

A second way of considering environments is to look at worst-case situations. In addition to Table B-1, several worst-case estimates of the parameters have been made for the geosynchronous environment (Table I-1). These values were derived from fits to actual plasma distributions observed during the several known worst-case ATS-6 and SCATHA charging events. The SCATHA spacecraft instrumentation allowed a breakout of the data into components parallel and perpendicular to the magnetic field and thus permitted a more realistic representation of the actual environment. These values are particularly useful in estimating the extremes in environment that a geosynchronous spacecraft is likely to encounter and are described in Appendix I.

A third quantity of interest in estimating the effects of the space environment on charging is the yearly percentage of occurrence of the plasma parameters. The occurrence frequencies of the temperature and current (Fig. B-1) were derived by fitting the observed distributions of electron and ion temperature for UCSD instruments on ATS-5, ATS-6, and SCATHA. The figures are useful in estimating the time during the year that a specified environment might be expected.

Table B-1. Average parameters from referenced spacecraft.

Parameter	ATS-5	ATS-6	SCATHA
Electron Parameters			
Number density (cm^{-3})	0.80	1.06	1.09
Current density ($\text{nA}\cdot\text{cm}^{-2}$)	0.068	0.096	0.115
Energy density ($\text{eV}\cdot\text{cm}^{-3}$)	1970	3590	3710
Energy flux ($\text{eV}\cdot\text{cm}^{-2}\cdot\text{s}^{-1}\cdot\text{sr}^{-1}$)	0.98×10^{12}	2.17×10^{12}	1.99×10^{12}
Number density for population 1 (cm^{-3})	0.578	0.751	0.780
Temperature for population 1 (keV)	0.277	0.460	0.550
Number density for population 2 (cm^{-3})	0.215	0.273	0.310
Temperature for population 2 (keV)	7.04	9.67	8.68
Average temperature (keV)	1.85	2.55	2.49
Root-mean-square temperature (keV)	3.85	6.25	4.83
Ion Parameters (Assumed to be Primarily H^+)			
Number density (cm^{-3})	1.36	1.26	0.58
Current density ($\text{pA}\cdot\text{cm}^{-2}$)	5.1	3.4	3.3
Energy density ($\text{eV}\cdot\text{cm}^{-3}$)	13,000	12,000	9,440
Energy flux ($\text{eV}\cdot\text{cm}^{-2}\cdot\text{s}^{-1}\cdot\text{sr}^{-1}$)	2.6×10^{11}	3.4×10^{11}	2.0×10^{11}
Number density for population 1 (cm^{-3})	0.75	0.93	0.19
Temperature for population 1 (keV)	0.30	0.27	0.80
Number density for population 2 (cm^{-3})	0.61	0.33	0.39
Temperature for population 2 (keV)	14.0	25.0	15.8
Average temperature (keV)	6.8	6.3	11.2
Root-mean-square temperature (keV)	12.0	23.0	14.5

Table B-2. Standard deviations.

Parameter Standard Deviation (\pm)	ATS-5	ATS-6	SCATHA
Electron Standard Deviations			
Number density (cm^{-3})	0.79	1.1	0.89
Current density (nA cm^{-2})	0.088	0.09	0.10
Energy density (eV cm^{-3})	3,100	3,700	3,400
Energy flux ($\text{eV cm}^{-2}\text{s}^{-1}\text{sr}^{-1}$)	1.7×10^{12}	2.6×10^{12}	2.0×10^{12}
Number density for population 1 (cm^{-3})	0.55	0.82	0.70
Temperature for population 1 (keV)	0.17	0.85	0.32
Number density for population 2 (cm^{-3})	0.38	0.34	0.37
Temperature for population 2 (keV)	2.1	3.6	4.0
Average temperature (keV)	2.0	2.0	1.5
Root-mean-square temperature (keV)	3.3	3.5	2.9
Ion Standard Deviations (Assumed to be Primarily H⁺)			
Number density (cm^{-3})	0.69	1.7	0.35
Current density (pA cm^{-2})	2.7	1.8	2.1
Energy density (eV cm^{-3})	9,700	9,100	6,820
Energy flux ($\text{eV cm}^{-2}\text{s}^{-1}\text{sr}^{-1}$)	3.5×10^{11}	3.6×10^{11}	1.7×10^{11}
Number density for population 1 (cm^{-3})	0.54	1.78	0.16
Temperature for population 1 (keV)	0.30	0.88	1.0
Number density for population 2 (cm^{-3})	0.33	0.16	0.26
Temperature for population 2 (keV)	5.0	8.5	5.0
Average temperature (keV)	3.6	8.4	4.6
Root-mean-square temperature (keV)	4.8	8.9	5.3

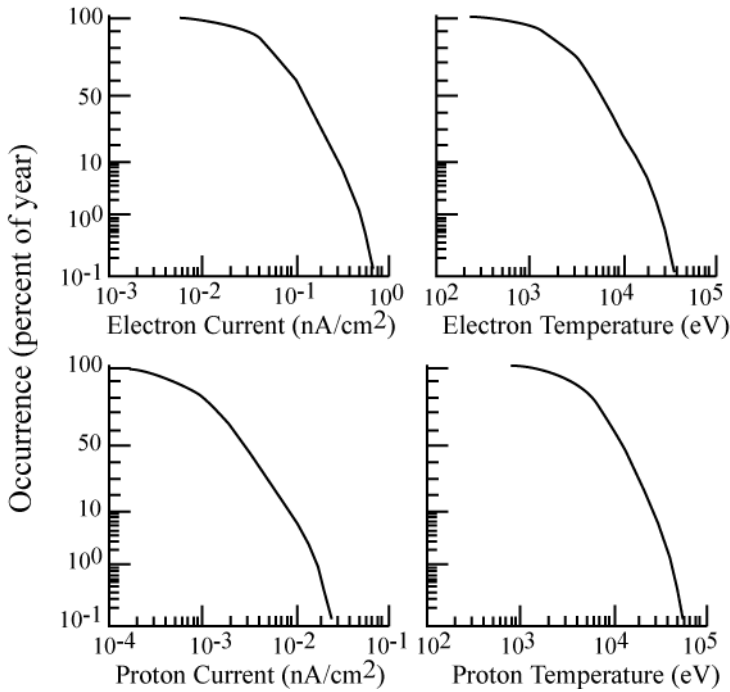


Fig. B-1. Occurrence frequencies of geosynchronous plasma parameters [15].

The fourth and a very important quantity of interest is how the plasma parameters vary with time during a charging event. The approaches determining this quantity range from detailed models simulating the magnetosphere to averages over many geomagnetic storms. For design purposes, we have adopted a simulation of the electron and proton current and temperature that approximates the natural variations in the potential as predicted by charging analysis codes. A time-history sequence suitable for modeling the worst effects of a geomagnetic storm is presented in Fig. B-2.

B.2.2 Geosynchronous High-Energy Environments

Unlike the plasma environment, the high energy electron geosynchronous environment (GEO) is perhaps the most well characterized of Earth orbits because of its importance for communications satellites. Quantitative data for GEO are more readily available than for other orbits. There are, however, a number of characteristics of the environment that need to be considered. These range from variations with longitude to rapid time-dependent variations in the high-energy electron spectra. Each of these is discussed below.

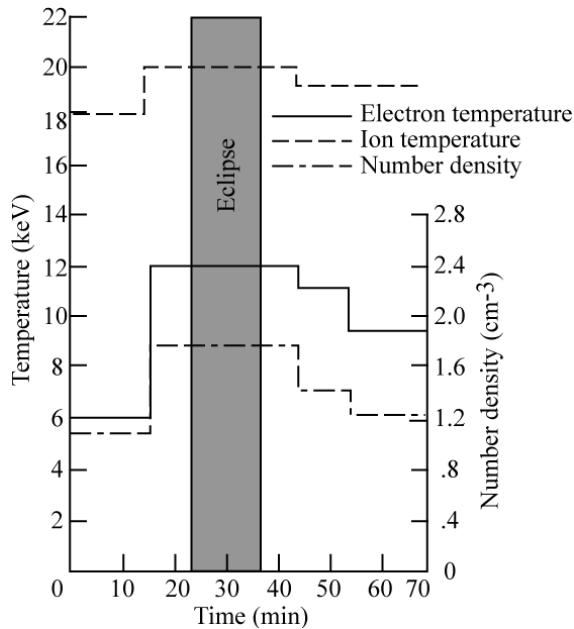


Fig. B-2. Suggested time history for simulating a substorm [15].

B.2.2.1 Variation with Solar Cycle

The high energy electron population at GEO has a long-term variation with the solar or, more commonly, the sunspot cycle (about 11 years). The $E > 2$ MeV electron population as measured by the geosynchronous GOES-7 satellites is roughly anti-correlated with the sunspot cycle; when the solar sunspot number is low, the GOES $E > 2$ MeV electron flux is high. This is shown in Figs. B-3 [16] and B-4.

Flying a mission at solar maximum would imply a lower mission (>2 MeV) fluence/dose. Unfortunately, most GEO missions nowadays have durations much longer than 5 years; therefore, for projects with an unknown launch date, the satellite should be designed to withstand the worst of these periods. This can be a problem, however, as the range between the worst-case conditions and the least stressing is more than 100:1 in energetic electron flux. However, the Sun, which drives these environments, does not strictly obey averages, and even during times when the >2 MeV electron fluxes are usually low, the energetic electron fluxes can be extremely high. The project manager, knowing the mission schedule, may wish to assume some risk to save project resources but the authors advise against such a strategy.

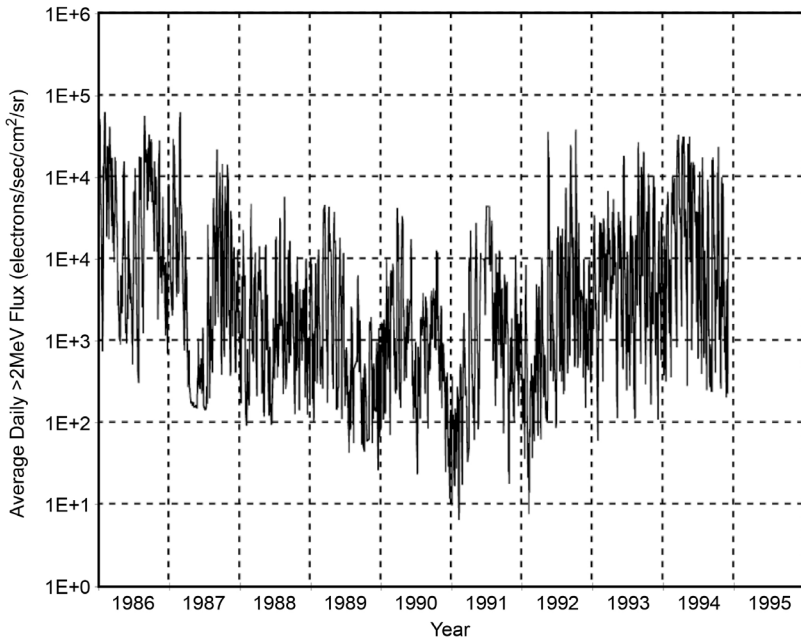


Fig. B-3. Average flux at geosynchronous orbit for E >2 MeV electrons as measured by the GOES spacecraft over ~one solar cycle (1986-1995).

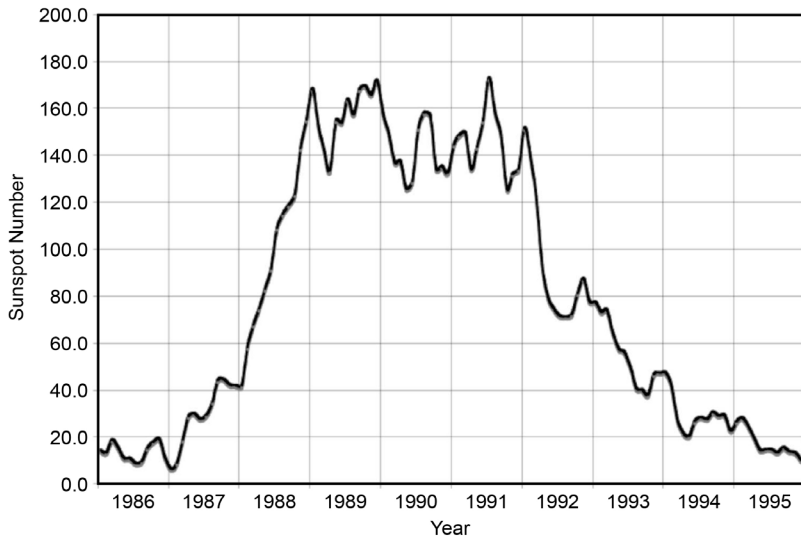


Fig. B-4. Observed and predicted smoothed sunspot numbers for 1986-1995 (monthly 3-month smoothed north sunspot number).

B.2.2.2 Variation with Longitude

The plasma/radiation environment is linked to Earth's magnetic field lines. Magnetic field lines are described in terms of L-value, the distance that a given magnetic field line crosses the magnetic equator in Earth radii (referenced to a dipole magnetic field model). Following a particular field line as it rotates around Earth traces out a surface called an L-shell. As charged particles (electrons, protons, etc.) are trapped to first order on a magnetic field line/L-shell, the radiation flux can be described in terms of the magnetic field strength at the observation point and the L-shell that passes through the point; this B-L coordinate system is often used in modeling radiation belts. Because Earth's magnetic dipole is tilted and offset with respect to the Earth's rotational axis, real Earth B-L values vary in longitude around geosynchronous orbit (Fig. B-5 [17]). Because the radiation environment is approximately constant on a particular L-shell at the magnetic equator, there is a change in the radiation environment at different longitudes as different B-L values are encountered at GEO altitudes. The corresponding fluence and dose variations at GEO are shown in Fig. B-6 [18].

The GEO electron fluences in Fig. B-6 are for the AE8 model, while the dose from electrons is for the CRRESRAD model. This figure is shown only to illustrate the average longitudinal variation. The maximum electron environment should be used for all satellites, even if their longitudinal location is known.

B.2.2.3 Variation with Averaging Interval

In addition to long-term solar cycle variations, there are short-term temporal variations associated with geomagnetic activity and rapid changes in Earth's magnetosphere. As a consequence, the average high-energy electron flux varies with the time interval over which the averaging is carried out. This can be seen when a large data set, gathered with a high time resolution, is averaged over increasingly longer integration times. The GOES E >2 MeV electrons are returned with a 5 min resolution. The variation between the daily peak flux determined in a 5 min interval to the peak flux average in a 24 hr period is about 3 to 4 (the 24 hr average peak is, as would be expected, lower). This issue of averaging interval should be kept in mind when comparing different data sets. Analysis of Fig. B-3 data from Herbert Sauer gives a similar answer (Fig. B-7).

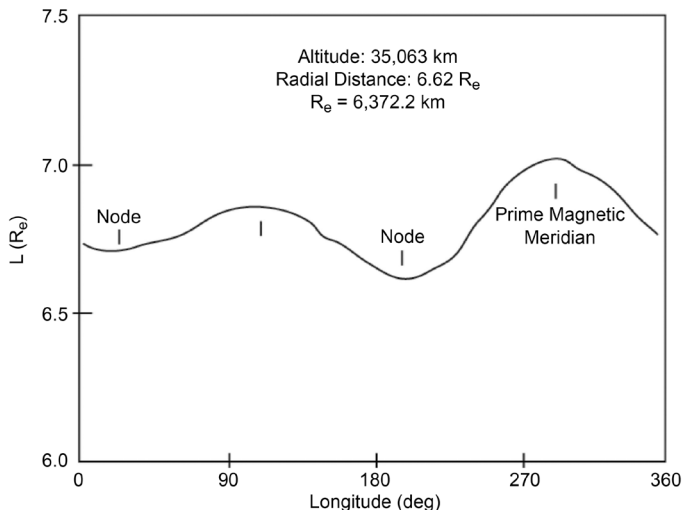


Fig. B-5. L-shell values (units of Earth radii) around Earth's Equator (0 deg Latitude) versus east longitude.

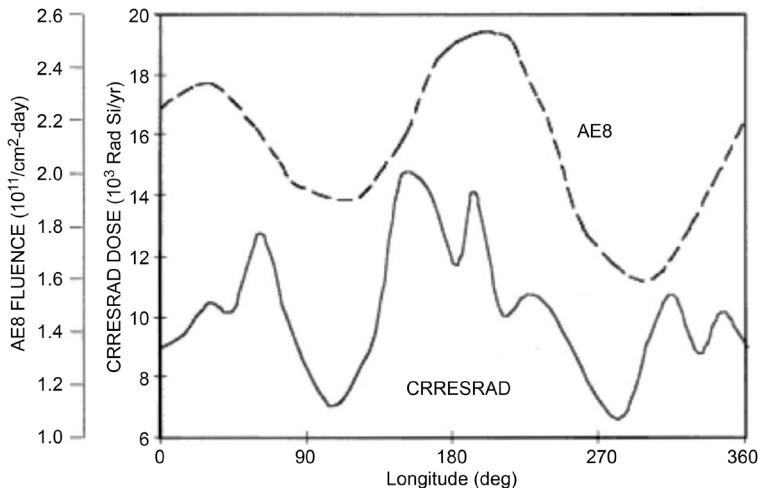
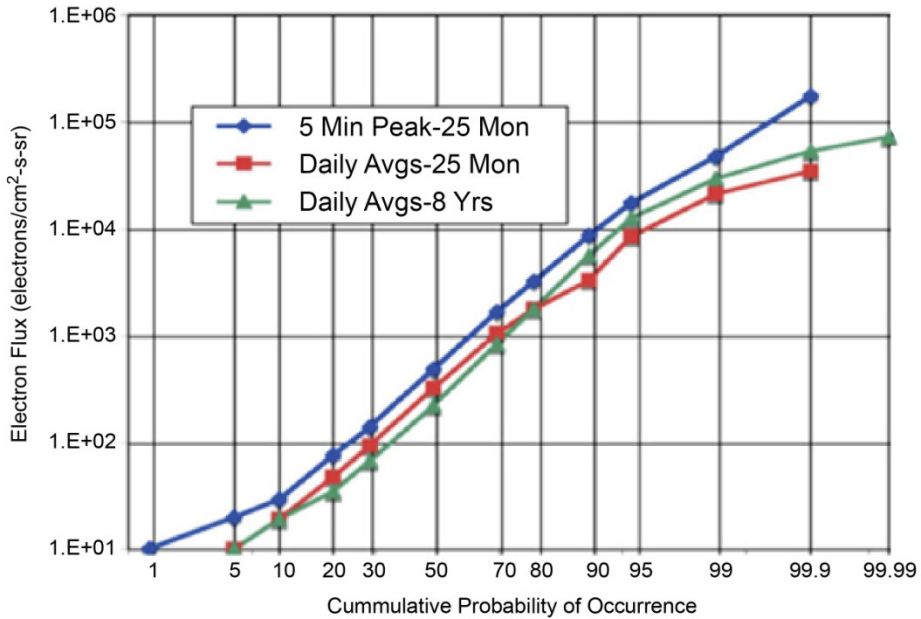


Fig. B-6. AE8 >0.5 MeV daily electron fluence and CRRESRAD annual dose caused by >1-MeV electrons plotted as functions of satellite east longitude at 6.6 R_e for the AE8 (>0.5 MeV) and CRRESRAD (>1 MeV) models.

B.2.2.4 Variation with Local Time

The high energy electrons at a given geosynchronous longitude vary daily with local time. On active days, the flux variation is about 10:1 from local noon to local midnight, with the highest flux near local noon. (The NOAA web site, <http://www.sec.noaa.gov/today.html>, shows the current 5-min electron flux at GEO for the last 3-day interval). The normal 24-hr average of the GOES



Key:

● Largest 5-min GOES flux in a day for active period*

■ GOES daily average flux for active period*

▲ GOES daily average flux for 8 yr (1/1/86 – 11/30/94)

*Selected from 25 continuous months at high levels (GEO, 1/1/92 – 1/31/94)

Fig. B-7. Cumulative probability of occurrence of GOES-7 $E > 2$ MeV electron fluxes for several different assumptions.

$E > 2$ MeV electron flux ($\text{e}\cdot\text{cm}^{-2}\cdot\text{s}^{-1}\cdot\text{sr}^{-1}$) is about one-third of the peak daily flux (the highest flux in a 5 min period) in these plots.

B.2.2.5 Spectrum

The integral electron spectrum varies with time in both shape and amplitude. Figure 2-6 presents a worst-case high-amplitude energy spectrum from the LANL SOPA detectors averaged over a few hours compared with a spectrum predicted by the AE8 model, which is a long-term average. Data from the AE8 average show a different spectral shape as well as lower amplitudes. That is, the ratio of integral electron flux at 2 MeV to that at 600 keV is generally not the same from day to day. It can be seen that, whereas at low energies ($E < 100$ keV), the curves approach each other, above 1 MeV the spectra rapidly diverge, with the worst-case spectrum approximately 2 orders of magnitude higher than the AE8 spectrum. This large difference between nominal, time-averaged, and short-term worst-case conditions is characteristic of the radiation environment at Earth. The AE8 model, because of its long-term averaging

interval (~5 year), is inappropriate for internal charging calculations as the effects typically are on the order of days or less. The effects of radiation-induced conductivity have not been included in the statements above. Radiation-induced conductivity will reduce the internal electric field. The effect may become noticeable at ~2 MeV, but not enough material data are available to make use of that fact.

B.2.2.6 Amplitude Statistics

An excellent set of data for the statistical analysis of the long-term variations in the total electron flux at geosynchronous orbit is that from the NOAA GOES-7. The data are only available for electrons for $E > 2$ MeV, but the measurements are from one detector and available for approximately one complete solar cycle (Fig. B-3). Figure B-7 plots the cumulative probability of occurrence of GOES-7 electron fluxes. The time span was an 8-year period encompassing the largest energetic fluxes in that solar cycle. Figure B-7 shows amplitude statistics for three statistics from that data set as follows:

- a. For the worst 25 months, the day's highest 5-min average flux.
- b. For the worst 25 months, the daily average flux.
- c. For the whole 8 year, the daily average flux.

The circles are the peak GOES electron flux data (largest amplitude 5 min value in the day) for times of higher flux (January 1, 1992, through January 31, 1994). The triangles correspond to the cumulative probability for the daily GOES average fluxes over the 8-year span from 1986 to 1994. The squares correspond to the GOES data for all daily averages from January 1, 1992, through January 31, 1994. All data are from [16]. The key feature to be noted here is that a Gaussian probability distribution implied by a straight-line fit from about 10 percent to about 95 percent does not explain the data above the 95th percentile. This makes it difficult to extrapolate with any confidence to a 99.99 percentile environment. The fall-off at the higher percentiles is real [19]. Thus, the worst environments, although real, are less frequent than a simple Gaussian distribution would imply. The reader is cautioned about trying to use these probabilities for design purposes; use the worst-case energy spectrum of Fig. 2-6.

B.3 Other Earth Environments

B.3.1 MEO

Medium Earth orbit (MEO) ranges from roughly 2,000 to 25,000 km altitude (1240 to 15,500 mi) with an electron flux peak at ~20,000 km (12,400 mi) altitude (the inner electron belt). For internal charging, it is the most stressing

of the Earth environments. As the Global Positioning Satellite (GPS), as well as some of the proposed multi-spacecraft communications systems, fly in this orbit, it is a major environment of concern in the study of internal charging phenomena. Figure B-8 (adapted from [20]) is a meridional schematic of Earth's radiation belts at 0 deg longitude showing the AE8 and AP8 predictions of the electron ($E > 1$ MeV) and proton ($E > 10$ MeV) fluxes. This plot clearly shows the two-belt structure of the electron belts and the horns that extend down to lower altitudes (the poles). It gives a clear picture of the MEO environment and how it is related to orbital characteristics. Each region has a unique spectrum associated with it, which would affect internal charging calculations. It should also be noted that a third electron belt can sometimes appear between the two main belts after severe geomagnetic storms. This belt can last for months before disappearing.

Note: Fig. B-8 shows both electron and proton fluxes as referenced to Earth's idealized dipole magnetic coordinates, combined onto one chart. The vertical axis is the pole axis with vertical units of Earth radii. The horizontal scale is magnetic equatorial distance from the axis in Earth radii. The upper half-chart represents protons; the southern hemisphere proton flux is a mirror image. The electrons (lower half-chart) also are symmetric above and below the magnetic equator in this coordinate system.

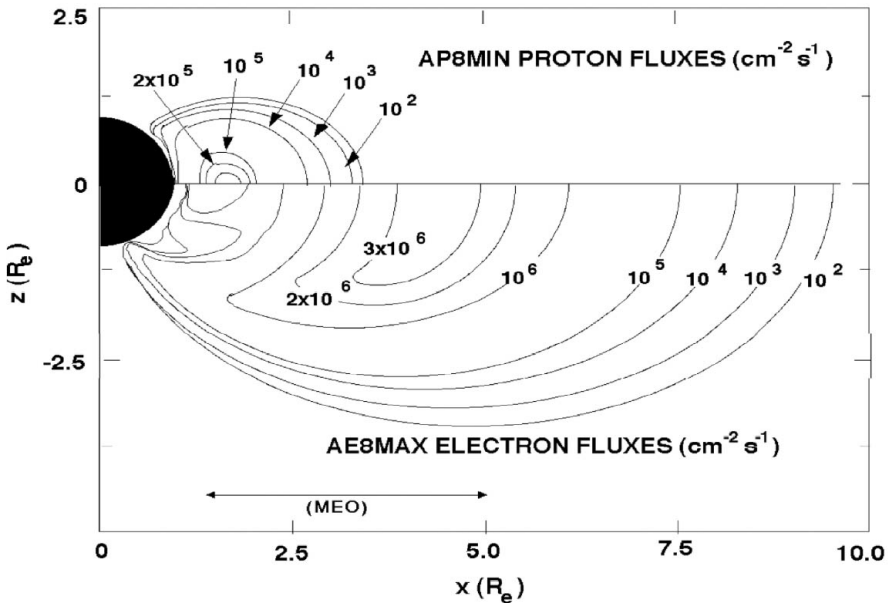


Fig. B-8. Schematic of Earth's radiation belts as estimated by the AE8 and AP8 models; contours for $E > 1$ MeV electrons and $E > 10$ MeV protons for 0 deg Longitude.

B.3.2 PEO

A second important orbital regime is that associated with highly inclined polar orbits. As seen in Fig. B-8, a polar orbit at low altitudes can pass through the horns of the electron belts and experience a significant, if short duration, flux of high-energy electrons. Many military spacecraft, most imaging spacecraft, and low-altitude communications fleets are in polar orbits. For low-altitude orbits (<1000 km [620 mi]), the risk of internal charging is present but generally much lower than at GEO or MEO. At higher altitudes, the interaction is dependent on the details of the orbit and can be minimized with a proper choice of eccentricity and inclination. Even so, any high-inclination orbit should be evaluated for potential internal charging issues early in the mission design.

B.3.3 Molniya Orbit

Another common orbit for Russian spacecraft is the so-called Molniya orbit. A Molniya orbit follows an elliptical track with a perigee of 500 km (310 mi) and an apogee of 39,000 km (24,000 mi). This orbit is inclined at 63 deg, and the period is on the order of 12 hours. As a spacecraft spends most of its time at apogee, this orbit provides good ground coverage for long periods of time at high latitudes, e.g., over Russia. In this orbit, satellites traverse a full range of space environments from the higher density, low-energy plasma at LEO through the radiation belts to interplanetary environments. The orbit is also exposed to light and dark so that the satellite is subjected to all environmental variations. Again, the high-energy electron environment should be evaluated for possible internal charging issues for Molniya missions.

B.4 Other Space Environments

B.4.1 Solar Wind

Aside from the energetic particle doses from sporadic solar proton events (SPEs) which are not particularly relevant to either surface or internal charging, the solar wind environment is relatively benign for most spacecraft charging applications. The solar wind is a fully ionized, electrically neutral, magnetized plasma that flows outward from the Sun. Table B-3 [21] summarizes many of the characteristics of the solar wind in the ecliptic plane. Perhaps not clear from the table is that the solar wind is highly variable and is coupled to the 11-year solar cycle of activity. Recent years have seen the creation of an interplanetary system of solar wind weather stations designed to closely monitor both solar and solar wind activity, e.g., Ulysses, WIND, Solar and Heliospheric Observatory (SOHO), Yohkoh Observatory, Advanced Composition Explorer (ACE), and the Transition Region and Coronal Explorer (TRACE). One of these, Ulysses, has flown over the poles of the Sun and mapped the solar wind

in three dimensions. These spacecraft have identified a variety of characteristic features associated with the solar wind plasma. Of particular interest are the so-called coronal mass ejection (CME) events and the high-speed solar wind streams as these tend to dominate what might be termed extreme conditions. These are illustrated in Fig. B-9 [22] and demonstrate the variability of the solar wind. It has, indeed, proven difficult, if not impossible, to define one or two worst-case solar wind charging environments, given the rich variety of plasma conditions and the potentially unique charging response of any given spacecraft design to those environments.

Minow, Parker, and their colleagues have carried out an in-depth review of the Ulysses and similar data solar wind data. They have generated reference spectra for the solar wind electron and proton environments from the Ulysses data in terms of frequency of occurrence percentiles (Fig. B-10 [23]). These spectra can be used to estimate surface and internal charging in the solar wind. As this level of detail is not needed in general for the surface charging studies, Maxwell-Boltzmann distributions can be assumed instead. Representative solar wind parameters under this assumption are tabulated for 1 AU and 0.5 AU in Table B-4. (Note: For simplicity, only the core population for the solar wind electrons was considered, while the electron halo population was ignored.) Nominal solar wind properties for these two environments are listed in Table B-4.

Table B-3. Characteristics of the solar wind at 1 AU in the Ecliptic Plane [21].

Property	Min	Max	Avg
Flux (#/cm ² -s)	10 ⁸	10 ¹⁰	2 to 3 × 10 ⁸
Velocity (km/s)	200	2500	400 to 500
Density (#/cm ³)	0.4	80	5 to >10
Temperature (eV)	0.5	100	20
T _{max} /T _{avg}	1.0 (isotropic)	2.5	1.4
Helium Ratio (N _{He} /N _H)	0	0.25	0.05
Flow Direction	±15 deg from radial		~2 deg East
Alfven Speed (km/s)	30	150	60
B, nT	0.25	40	6
B Vector	Polar Component		Average in ecliptic plane
	Planar Component		Average in spiral angle ~45 deg

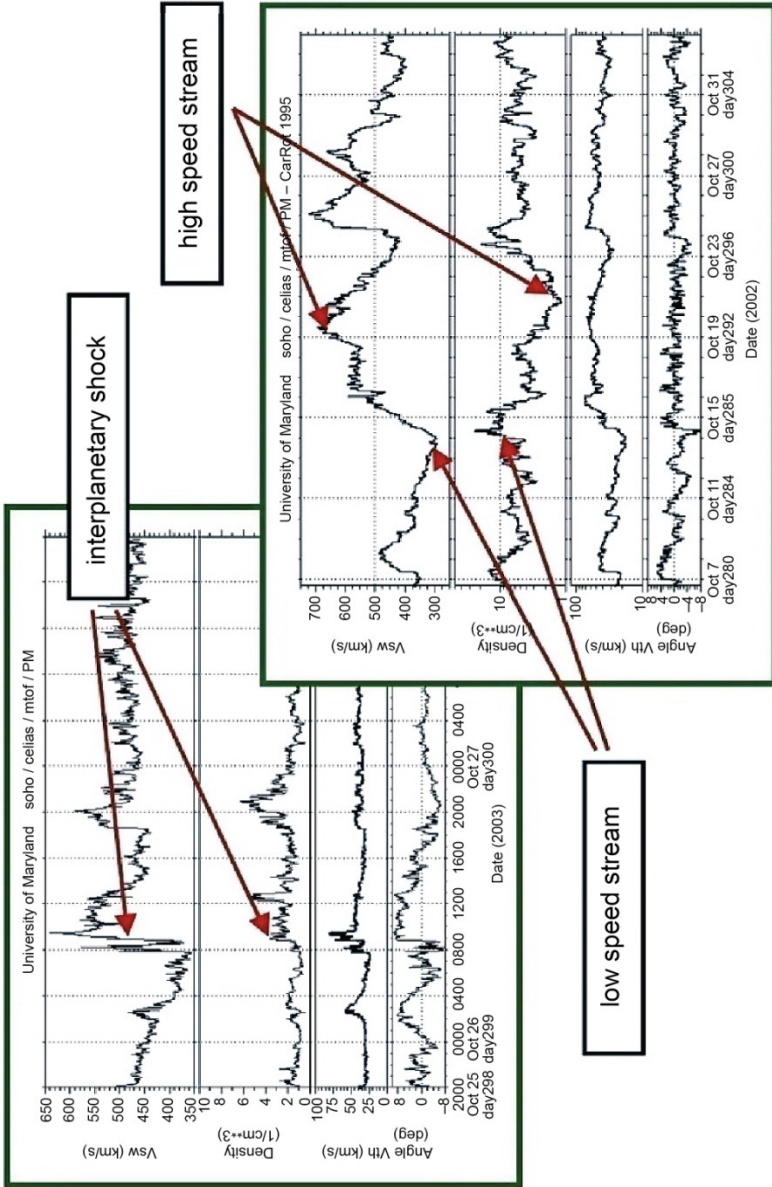


Fig. B-9. Solar wind parameters for an interplanetary shock and high- and low-speed stream versus time as measured by the SOHO spacecraft (Garrett and Minow, 2007 [22]; SOHO CELIAS/Proton Monitor data courtesy of University of Maryland).

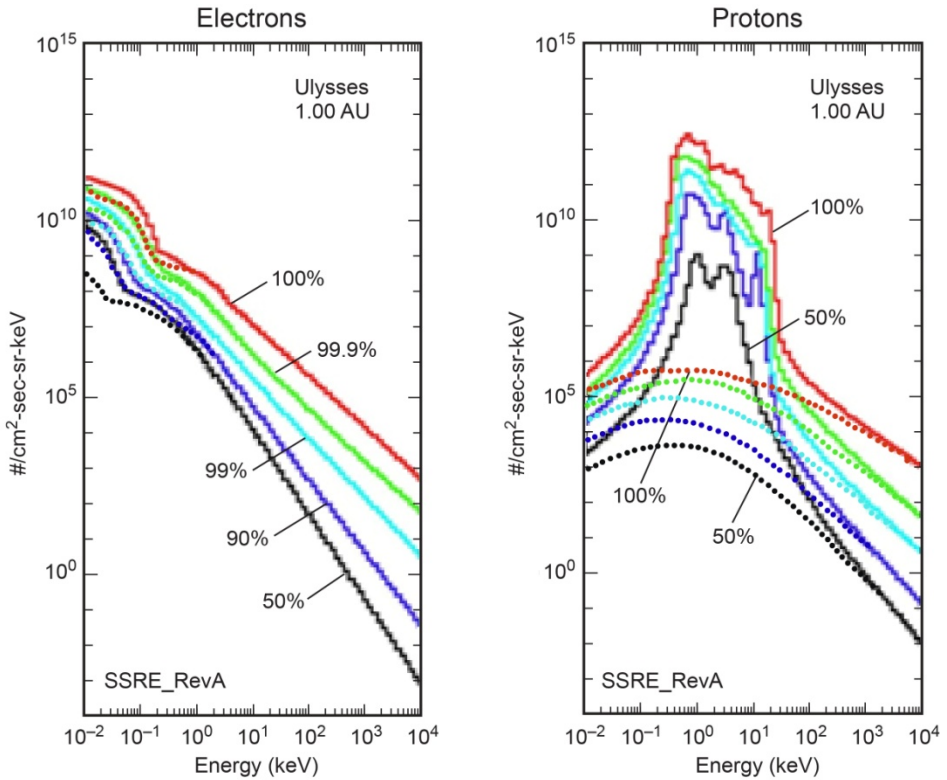


Fig. B-10. Solar wind particle spectra based on measurements made by the Ulysses spacecraft for environments of various probability. The solid lines represent flows from the Sun; dashed lines represent flows toward the Sun [23].

B.4.2 Earth, Jupiter, and Saturn Magnetospheres Compared

Table B-5 lists the principal characteristics of the terrestrial, jovian, and saturnian magnetospheres. Jupiter and Saturn are roughly 10 times the size of Earth while their magnetic moments are, respectively, 2×10^4 times and 500 times larger. As the magnetic field at the Equator is proportional to the magnetic moment divided by the cube of the radial distance, the terrestrial and saturnian magnetospheres scale similarly in terms of planetary radii. The jovian magnetic field, however, is 20 times proportionally larger. An additional consideration is that the photoelectron flux at 1 AU for the Earth is ~ 25 times that at Jupiter (~ 5 AU) and ~ 100 times that at Saturn (~ 10 AU).

Table B-4. Nominal solar wind plasma environments.

Plasma Environment	0.5 AU	1.0 AU
RE (cm ⁻³)	17	12.8
TE (eV)	10.6	11.13
RI (cm ⁻³)	17	12.8
TI (eV)	40	10
Photoelectron Current (CPH) (nA/cm ²)	8	2
Bulk Flow Velocity (km/s)	702	327
Potentials (estimated):	0.5 AU	1.0 AU
Shadowed (insulator)	-22	-22.6
Sunlight (conductive)	11.7	7.5

RE: density for electron plasma population
 TE: temperature for electron plasma population
 RI: density for ion plasma population
 TI: temperature for ion plasma population

Table B-5. The magnetospheres of Earth, Jupiter, and Saturn.

Planet	Region/Parameter			
	Equatorial Radius (km) mi	Magnetic Moment (G-cm ³)	Rotation Period (hr)	Aphelion/Perihelion (AU)
Earth	6.38 × 10 ³ 3960	8.10 × 10 ²⁵	24.0	1.01/0.98
Jupiter	7.14 × 10 ⁴ 44,400	1.59 × 10 ³⁰	9.925	5.45/4.95
Saturn	6.00 × 10 ⁴ 37,000	4.30 × 10 ²⁸	10.23	10.06/9.01

The rotation rate is also an important factor. Both Jupiter and Saturn spin over twice as fast as Earth (~10 hour versus 24 hr). Given their strong magnetic fields, this means that the cold plasma trapped in these magnetospheres is forced to co-rotate at velocities much higher than a spacecraft’s orbital velocity. This is opposite the situation at Earth where, at low altitudes, a spacecraft orbits at ~8 km/s faster than the ionospheric plasma. Co-rotation velocities can range from 30 to 40 km/s near Jupiter and Saturn to over 100 km/s in their outer magnetospheres. As the magnetosphere is the primary controlling factor for the local plasma environments, the charging environment differs considerably for each of these planets.

The magnetosphere of Jupiter is dominated by the following three factors:

- a. The magnetic field tilt (11 deg) relative to its spin axis.
- b. Its rapid rotation.
- c. The jovian moon Io at 5 R_j.

Io generates a vast torus of gas. The rapid rotation of Jupiter's magnetic field forces the cold plasma associated with this torus to accelerate and expand by centrifugal force into a giant disc. The magnetic field tilt and rotation rate make this plasma disc move up and down so, at a given location, plasma parameters vary radically over a 10-hour period (or 5 hours in the plasma sheet). Jupiter's environment can be roughly divided into the following three populations:

- a. The cold plasma associated with the Io torus and the plasma disc ($0 < E < 1$ keV).
- b. The intermediate plasma and aurora ($1 \text{ keV} < E < 100$ keV).
- c. The radiation environment ($E > 100$ keV).

The cold plasma environment has high densities ($\sim 2000 \text{ cm}^{-3}$) and low energies (1 eV to 1 keV). This plasma consists of hydrogen, oxygen (singly and doubly ionized), sulfur (singly, doubly, and triply ionized), and sodium (singly ionized) ions. The intermediate plasma environment is made up of electrons (~ 1 keV) and protons (~ 30 keV) and assumed to vary exponentially from $\sim 5 \text{ cm}^{-3}$ for $r < 10$ R_j to 0.001 cm^{-3} beyond 40 R_j. Co-rotation velocities vary from ~ 45 km/s at 4 R_j to ~ 250 km/s at 20 R_j.

Saturn is marked by a magnificent set of rings that are its most obvious feature and set it apart from all the other planets. Aside from the rings, however, Saturn's magnetosphere resembles Jupiter's—a cold inner plasma disk giving way to a lower density, slightly higher energy plasma disk at large distances. Although there is no Io-equivalent moon in the inner magnetosphere, there is still a fairly dense cold plasma sheet and, at ~ 20 R_s, Saturn's huge moon Titan contributes a large cloud of neutral gas in the outer magnetosphere. Unlike Jupiter, Saturn's magnetic field axis is apparently aligned with the spin axis so that the plasma ring around Saturn is relatively stable compared to that of Jupiter. Plasma co-rotation velocities are similar to those of Jupiter, though maximum velocities tend to peak a little above 100 km/s.

A simple design tool based on current balance and on Earth's, Jupiter's, and Saturn's cold and intermediate plasma environments (the latter also includes the aurora that have been observed at all three planets) has been used to estimate

the spacecraft-to-space potentials for these planets. The results of this tool for a spherical spacecraft with aluminum surfaces are presented in Table B-6 for several different plasma regions and situations.¹ Based on this table, Earth clearly represents the worst threat to spacecraft. Negative potentials as high as 20,000 V are predicted near geosynchronous orbit in eclipse, and, indeed, potentials in excess of -20,000 V have apparently been observed. At Jupiter, potentials are more moderate. Large potentials are only observed if secondary emissions can be suppressed, unlikely but possible for some surface configurations. Conditions at Saturn are similar to those at Jupiter, though somewhat lower in general. Even so, spacecraft surface charging is still a concern for spacecraft survivability at these planets. Indeed, as potentials of even a few tens of volts can seriously affect low-energy plasma measurements, spacecraft charging should be considered for scientific missions to these planets.

The high-energy electrons that are part of the radiation environment at each of the three planets are the source of internal charging. In Fig. B-11, the 1 MeV electron flux contours for Earth (AE8Max model), Jupiter (Galileo Interim Radiation Electron (GIRE) model), and Saturn (Saturn Radiation (SATRAD) model) are presented. In a number of studies [24,25], it has been demonstrated that fluences of 10^{10} electrons/cm² are roughly the level required for an IESD. The fluxes in the most intense regions in Fig. B-11 are on the order of 10^7 , 10^8 , and 10^6 electrons/cm²-s for Earth, Jupiter, and Saturn, respectively. (Note: the inner radiation belt at Saturn is largely missing because of Saturn's ring system.) This implies internal charging times for 1 MeV electrons of $\sim 10^3$ s, $\sim 10^2$ s, and $\sim 10^4$ s. Flight experience has shown that the Earth poses moderate to severe IESD problems, Jupiter has severe IESD, and Saturn has not demonstrated any problems to date in agreement with these charging times.

¹ Insoo Jun of Jet Propulsion Laboratory, Pasadena, California supplied this material in a personal communication in 2006.

Table B-6. Representative charging levels (volts) at Earth, Jupiter, and Saturn based on a simple charging design tool.

Region	Plasma Convection Velocity Vc (km/s)	Potential (in Sunlight)	Potential (No Sun/No Secondaries)
Earth			
Ionosphere	8	-0.7	-4.4
Plasmasphere	3.7	-1.6	-3.8
auroral zone	8	-0.7	-500
Geosynchronous	3	2.0	-20,000
Jupiter			
cold torus	44	-0.59	-1.2
hot torus	100	-60	-70
plasma sheet	150	-94	-130
outer magnetosphere	250	9.5	-2,500
Saturn			
inner plasma sheet	40	~5	-30
outer plasma sheet	80	~5	-500
hot outer magnetosphere	100	-100	-500

References

- [1] H. B. Garrett and S. E. DeForest, "Analytical Simulation of the Geosynchronous Plasma Environment," *Planetary and Space Science*, vol. 27, pp. 1101-1109, 1979.
- [2] H. B. Garrett, D. C. Schwank, and S. E. DeForest, "A Statistical Analysis of the Low-energy Geosynchronous Plasma Environment--I. Electrons," *Planetary and Space Sciences*, vol. 29, pp. 1021-1044, 1981.
- [3] H. B. Garrett, D. C. Schwank, and S. E. DeForest, "A Statistical Analysis of the Low-energy Geosynchronous Plasma Environment--II. Ions," *Planetary and Space Sciences*, vol. 29, pp. 1045-1060, 1981.
- [4] H. B. Garrett, D. C. Schwank, P. R. Higbie, and D. N. Baker, "Comparison Between the 30-80 keV Electron Channels on ATS-6 and 1976-059A During Conjunction and Application to Spacecraft Charging Prediction," *Journal of Geophysical Research*, vol. 85, no. A3, pp. 1155-1162, 1980.

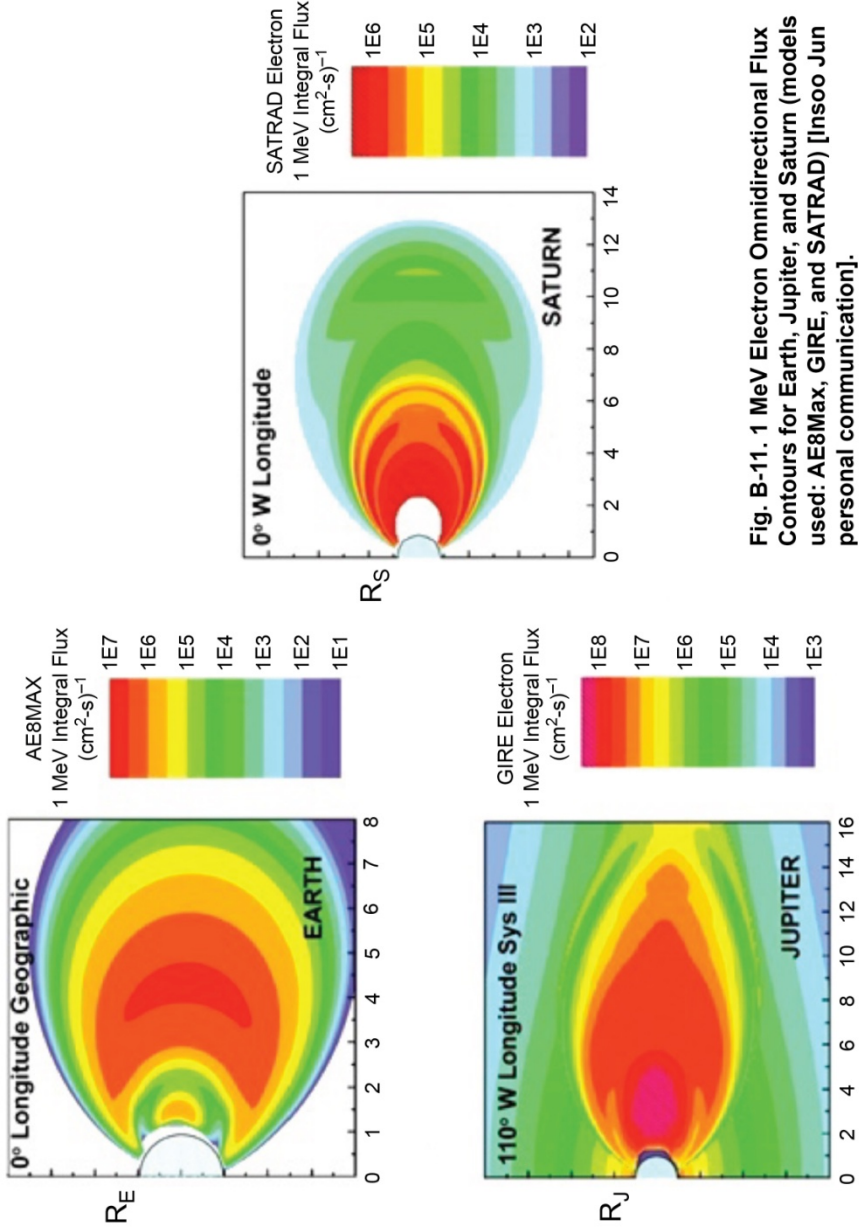


Fig. B-11. 1 MeV Electron Omnidirectional Flux Contours for Earth, Jupiter, and Saturn (models used: AE8Max, GIRE, and SATRAD) [Insoo Jun personal communication].

- [5] A. Jursa, ed., *Handbook of Geophysics and the Space Environment*., 4th edition, Air Force Geophysics Laboratory, Hanscom Air Force Base, Massachusetts, National Technical Information Service Document, Accession No. AD-A167000, December 5, 1985.
Additional reading for the space environment and interactions with spacecraft. An excellent reference for Earth space plasma environments as well as many other space environments.
- [6] E. G. Mullen and M. S. Gussenhoven, "SCATHA Environmental Atlas," AFGL-TR-83-0002, AFGL, Hanscom Air Force Base, Massachusetts, 1983.
- [7] E. G. Mullen, M. S. Gussenhoven, and H. B. Garrett, "A 'Worst Case' Spacecraft Environment as Observed by SCATHA on 24 April 1979," AFGL-TR-81-0231, Air Force Geophysics Laboratory, Hanscom Air Force Base, Massachusetts, 1981.
- [8] E. G. Mullen, M. S. Gussenhoven, D. A. Hardy, T. A. Aggson, B. G. Ledly, and E. C. Whipple, "SCATHA Survey of High-Level Spacecraft Charging in Sunlight," *Journal of Geophysical Research*, vol. 91, no. A2, pp. 1474–1490, February 1, 1986.
- [9] E. G. Mullen, D. A. Hardy, H. B. Garrett, and E. C. Whipple, "P78-2 SCATHA Environmental Data Atlas," *Spacecraft Charging Technology 1980*, NASA CP 2182/AFGL-TR-81-0270, National Aeronautics and Space Administration, pp. 802–813, 1981.
- [10] D. M. Boscher, S. A. Bourdarie, R. H. W. Friedel, and R. D. Belian, "Model for the Geostationary Electron Environment," *IEEE Transactions on Nuclear Science*, vol. 50, no. 6, pp. 2278–2283, 2003.
- [11] A. Sicard-Piet, S. Bourdarie, D. Boscher, R. H. W. Friedel, M. Thomsen, T. Goka, H. Matsumoto, and H. Koshiishi, "A New International Geostationary Electron Model: IGE-2006, from 1 keV to 5.2 MeV," *Space Weather*, vol. 6, S07003, doi:10.1029/2007SW000368, 13 pp., 2008.
- [12] V. A. Davis, M. J. Mandell, and M. F. Thomsen, "Representation of the Measured Geosynchronous Plasma Environment in Spacecraft Charging Calculations," *Journal of Geophysical Research*, vol. 113, no. A10204, doi:10.1029/2008JA013116, 14 pp., 2008.
- [13] M. F. Thomsen, M. H. Denton, B. Lavraud, and M. Bodeau, "Statistics of Plasma Fluxes at Geosynchronous Orbit Over More than a Full Solar Cycle," *Space Weather*, vol. 5, S03004, doi:10.1029/2006SW00025, 9 pp., 2007.
- [14] K. A. Ryden, P. A. Morris, A. D. P. Hands, C. S. Dyer, M. Fellows, B. Taylor, C. I. Underwood, D. J. Rodgers, G. Mandorlo, G. Gatti, H. D. R. Evans, and E. J. Daly, "Radiation monitoring in Medium Earth Orbit over

the solar minimum period,” *Proceedings of RADECS 2008*, September 10–13, Jyvaskyla, Finland, 2008.

Reports and conclusions from data of Merlin experiment on Giove-A spacecraft (MEO, 23 km, 56 deg inclination) launched December 28, 2005. Compares to existing space radiation (electrons, dose, protons). Its references are a must-have.

- [15] C. K. Purvis, H. B. Garrett, A. C. Whittlesey, and N. J. Stevens, *Design Guidelines for Assessing and Controlling Spacecraft Charging Effects*, NASA Technical Paper 2361, National Aeronautics and Space Administration, September 1984.
This document has been widely used by practitioners of this art (usually EMC engineers or radiation survivability engineers) since its publication in 1984. Its contents are limited to surface charging effects. The contents are valid to this day for that purpose. NASA TP-2361 contents have been incorporated into this NASA-STD-4002, Rev A, with heavy editing. Many of the original details, especially time-variant and multiple-case versions of suggested environments, have been simplified into single worst-case environments in NASA-HDBK-4002, Revision A. Some background material has not been transferred into this document, so the original may still be of interest.
- [16] *GOES SEM Data Notes: Important Information for Data Users*, website, National Oceanic and Atmospheric Administration National Geophysical Data Center. <http://www.ngdc.noaa.gov/stp/satellite/goes/datanotes.html> (Website Accessed May 9, 2011.)
Herbert Sauer of the National Oceanic and Atmospheric Administration, National Geophysical Data Center (Boulder, Colorado) initially supplied this information to the authors in a personal communication. His data and that of others were later incorporated into the referenced website.
- [17] E. G. Stassinopoulos, “The Geostationary Radiation Environment,” *Journal of Spacecraft and Rockets*, vol. 17, no. 2, pp. 145–152, March-April 1980.
- [18] G. L. Wrenn, “Conclusive Evidence for Internal Dielectric Charging Anomalies on Geosynchronous Communications Spacecraft,” *Journal of Spacecraft and Rockets*, vol. 32, no. 3, May-June, pp. 514–520, 1995. Note that the author believes that there was still a need to convince people that internal charging was a real phenomenon, as recently as 1995.
- [19] C. F. Kennel and H. E. Petschek, “Limit on Stably Trapped Particle Fluxes,” *Journal of Geophysical Research*, vol. 71, pp. 1–28, 1966.
- [20] E. J. Daly, “The Evaluation of Space Radiation Environments for ESA Projects,” *ESA Journal*, vol. 12, pp. 229–247, 1988.

- [21] E. N. Parker, *Interplanetary Dynamical Processes*, Interscience, New York, New York, 1963.
- [22] H. B. Garrett and J. I. Minow, *Charged Particle Effects on Solar Sails*, NASA Report ISPT-SS-06-101, Marshall Space Flight Center, Huntsville, Alabama, 2007.
Figure B-9 is based on the CELIAS/MTOF experiment on the Solar Heliospheric Observatory (SOHO) spacecraft. SOHO is a joint mission of the European Space Agency and the National Aeronautics and Space Administration.
- [23] J. I. Minow, L. N. Parker, and R. L. Altstatt, “Radiation and Internal Charging Environments for Thin Dielectrics in Interplanetary Space,” presented at *The 9th Spacecraft Charging Technology Conference*, Tsukuba, Japan, April 2–9, 2005.
- [24] P. Leung, A. C. Whittlesey, H. B. Garrett, and P. A. Robinson, Jr., “Environment-Induced Electrostatic Discharges as the Cause of Voyager 1 Power-On Resets,” *Journal of Spacecraft and Rockets*, vol. 23, no. 3, May/June, pp. 323–330, 1986.
One of the best documented examples of IESD.
- [25] A. R. Frederickson, E. G. Holeman, and E. G. Mullen, “Characteristics of Spontaneous Electrical Discharges of Various Insulators in Space Radiation,” *IEEE Transactions on Nuclear Science*, vol. 39, no. 6, pp. 1773–1982, December 1992.
This journal paper is a description of the best-known attempt to quantify internal charging effects on orbit by means of a well-thought-out experiment design. The results were not all that the investigators had hoped, but the data are excellent and very good conclusions can be reached from the data, in spite of the investigators’ concerns.